Nanocomposites of cobalt sulfide embedded carbon nanotubes with enhanced supercapacitor performance

Hao Li[1], Zhijie Li[1*], Zhonglin Wu[1], Mengxuan Sun[1], Shaobo Han[2], Chao Cai[2], Wenzhong Shen[3], YongQing Fu[4**]

[1]School of Physics, University of Electronic Science and Technology of China, Chengdu, 610054, P. R. China

[2]Institute of Fundamental and Frontier Sciences, University of Electronic Science and Technology of China, Chengdu, 610054, P. R. China

[3]State Key Laboratory of Coal Conversion, Institute of Coal Chemistry, Chinese Academy of Science, Taiyuan, 030001, China

[4]Faculty of Engineering and Environment, Northumbria University, Newcastle Upon Tyne, NE1 8ST, UK

Abstract

CoS is one of the ideal electrode materials for supercapacitor, but its long-term stability and electrochemical performance needed to be improved before its successful application. Uniformly embedding carbon nanotubes (CNTs) inside the CoS matrix can provide numerous and effective diffusion paths of electrons and electrolyte ions, which can reduce the charge-transfer resistance and effectively improve the electrochemical performance of CoS. In this work, nanocomposites of $Co_2(CO_3)(OH)_2$ and CNTs were prepared using a facile hydrothermal method, and then were transformed into $CoS_{1.29}$@CNTs nanocomposites via an ion-exchange process. The carbon nanotubes were uniformly embedded inside the $CoS_{1.29}$ matrix. When the amount of CNTs was 6.1 wt%, the $CoS_{1.29}$@CNTs electrode exhibited a higher specific capacitance (99.7 mAh g^{-1}) than that of $CoS_{1.29}$ electrode (84.1 mAh g^{-1}) at a current density of 1 A g^{-1} measured in 2 M KOH electrolyte. The asymmetric supercapacitor assembled with the $CoS_{1.29}$@CNTs-6.1% electrode and an activated carbon (AC) electrode exhibited an energy density of 39.1 Wh kg^{-1} at a power density of 399.9 W kg^{-1}. Moreover, the specific capacitance of the $CoS_{1.29}$@CNTs-6.1%//AC device maintained 91.3 % of its original value after 2000 cycles at a current density of 3 A g^{-1}.

Key words:

Cobalt sulfide, Carbon nanotubes, Composites, Supercapacitor, Capacitance.

1. Introduction

In recent years, environmental pollution and shortage of fossil fuels have received worldwide attention, thus, research and design of pollution free and highly efficient energy storage systems are of particular significance [1, 2]. Because of their high power density, rapid charging/discharging ability and long cycle life, supercapacitors have been extensively studied [3, 4]. In terms of energy storage methods, there are only two types of supercapacitors. The first one is pseudocapacitor, which is based on Faradic reactions of the electrode materials; and the other one is electrical double-layer capacitors, which is based on charge absorption/desorption and diffusion at electrode/electrolyte interface [5]. Compared to the electrical double-layer capacitor, the pseudocapacitor usually exhibits much higher specific capacitance and energy density [6].

Many materials have been investigated to be used for the pseudocapacitor electrode, such as metal oxides, metal sulfides and conduction polymers [7]. Transition metal oxides/hydroxides and conductive polymers can produce much higher capacitance, but the poor cycle stability and low electric conductivity limit their applications in supercapacitors. Whereas metal sulfides such as CoS_2, Ni_3S_4, $Cu_{1.96}S$, MoS_2 and ZnS et.al have high reversible redox capability and low intrinsic resistance [8-14], and thus they have been considered as promising electrode materials. Among them, cobalt sulfide (Co_xS_y) has an excellent electrical conductivity and abundant redox reaction sites. It is regarded as one of the suitable candidates for electrode material, however, it is often suffered from poor performance during long-term charge/discharge processes [15].

It was reported that the electrochemical performance of metal sulfides can be effectively improved by addition of carbon materials including carbon nanotubes [16], carbon nanofibers [17], graphene [18] and carbon spheres [19]. The reason can be attributed to their low electron transfer resistances, high specific surface areas and stable electrical properties. For examples, rGO/CoS_2 exhibited a much better capacitive performance of 635.8 F g^{-1} at 1 A g^{-1} than that of pure cobalt sulfide [20]. The composite of $CoS_{1.097}$ with N-doped carbon matrix prepared using a chemical bath deposition and annealed under an Ar atmosphere demonstrated a specific capacitance of 360.1 F g^{-1} at 1.5 A g^{-1} [21]. The composite of cobalt sulfide/graphitic carbon nitride hybrid nanosheet was prepared using a simple solvothermal method, and it achieved a specific capacitance of 668 F g^{-1} at 2 A g^{-1} [22]. The electrochemical performance of these cobalt sulfides has been obviously improved by the addition of carbon materials. Compared with other carbon materials, carbon nanotubes have one-dimensional structure, which can provide an effective diffusion path for transport of electrolyte ions and charge transport to cause low value of charge-transfer resistance [16, 23]. Based on this, it is predicted that modification of cobalt sulfide using carbon nanotubes could improve the electrochemical performance of pseudocapacitors. For examples, Mohammadi et al prepared CNTs/Co_3S_4 composites using hydrothermal method [24]. Mao et al synthesized CoS_x/MWCNTs using hydrothermal method, in which the CoS and CoS_2 nanocrystals coated on functionalized multi-walled carbon nanotubes to form shell/core composite[25]. Chen et al prepared CNT/CoS composites using a precipitation process in the presence of poly(vinylpyrrolidone), in which the CoS was hexagonal nanocrystal in the

composites [26]. All these composites of cobalt sulfides/CNTs showed good electrochemical performance. However, the specific capacity of CNTs/Co_3S_4 composite is only 653 F g^{-1} at 1 A g^{-1}. The specific capacity of CoS_x/MWCNTs showed about 13% decay after 2000 cycles. The specific capacity of CNT/CoS decreased to 41% with the increase of scan rate from 1 to 100 mV s^{-1}. In these cobalt sulfides/CNTs composites, the cobalt sulfides (Co_3S_4, CoS and CoS_2) were nanocrystals. The composites of amorphous cobalt sulfides with CNTs have not been reported until now. In addition, the above cobalt sulfides/CNTs composites were obtained by addition of sodium thiosulfate, thioacetamide or thiourea in the preparation process. The method of transformation of $Co_2(CO_3)(OH)_2$@CNTs into cobalt sulfides@CNTs using a ion-exchange process in a Na_2S solution has not been reported.

In this work, $Co_2(CO_3)(OH)_2$@CNTs composite was prepared using a facile hydrothermal method, which was then transformed into $CoS_{1.29}$@CNTs-6.1% using an ion-exchange process in a Na_2S solution at 80 ^oC. The combination of CNTs and $CoS_{1.29}$ enhanced charge-transfer and ion diffusion rate, and increased the specific surface areas. The $CoS_{1.29}$@CNTs-6.1% achieved a much higher specific capacitance (99.7 mAh g^{-1}) than the pristine $CoS_{1.29}$ electrode (84.1 mAh g^{-1}). In addition, the assembled asymmetrical supercapacitor (ASC) using $CoS_{1.29}$@CNTs-6.1% and active carbon exhibited excellent energy and power densities. And the specific capacitance of the $CoS_{1.29}$@CNTs-6.1%//AC device maintained 91.3 % of its original value after 2000 cycles at a current density of 3 A g^{-1}.

2. Experimental details

2.1 Synthesis of $CoS_{1.29}$@CNTs composites

In the experiments, all the reagents were analytical grade and used without further purification. CNTs were synthesized using a conventional chemical vapor deposition (CVD) method [27]. Fig. 1 shows a schematic illustration of the fabrication process of $CoS_{1.29}$@CNTs. $CoS_{1.29}$@CNTs nanocomposites were prepared using a facile hydrothermal method, followed by an ion-exchange sulfuration process. Firstly, 50 mg of CNTs were dispersed in 20 mL deionized water and vigorous stirred for 20 min to form a liquid suspension. $Co(NO_3)_2 \cdot 6H_2O$ of 2.91 g and urea of 3.60 g were dissolved in 80 mL deionized water to form a pink solution. Secondly, the CNTs suspension was added into the above solution, and then was stirred for 30 min. The mixture was transferred into a 140 mL Teflon-lined autoclave and kept in an oven at 120 ^{o}C for 6 h. After cooled down to room temperature, the purple precipitate from the autoclave was washed using deionized water and dried at 60 ^{o}C for 8 h to obtain the $Co_2(CO_3)(OH)_2$@CNTs-6.1% composite.

To prepare the $CoS_{1.29}$@CNTs-6.1% composite, 0.1 g $Co_2(CO_3)(OH)_2$@CNTs-6.1% was added into Na_2S aqueous solution (30 mL and 0.4 mol L^{-1}) and stirred for 10 min. Then, the solution was kept at 80 ^{o}C for 24 h, and the obtained black sample was washed with deionized water and ethanol and dried in vacuum at 60 ^{o}C for 12 h. Utilizing the same procedures, the samples of $CoS_{1.29}$@CNTs-2.5%, $CoS_{1.29}$@CNTs-9.1% and pristine $CoS_{1.29}$ were also prepared by changing the additive amounts of CNTs to 20 mg, 80 mg and 0 mg, respectively.

2.2 Materials characterization

Morphology and micro/nanostructures of the materials were characterized using an scanning electron microscope (SEM, Inspect F50) and transmission electron microscope (TEM, JEOL 2010F with a field emission gun). Analysis using the energy-dispersive X-ray spectroscopy (EDX) was carried out to obtain the dot-mapping of various elements in nanocomposites. Chemical states of different elements of materials were obtained using an X-ray photoelectron spectroscope (XPS, ESCALAB 250Xi apparatus) with the Al kα as the excitation source and carbon C1s peak for calibrations of peak position. Fourier transform infrared (FT-IR) spectrum was obtained using an FT-IR transmittance spectrometer (Nicolet 6700, USA) with the wavelengths in the range of 400~4000 cm^{-1}. Raman spectrum was performed on an Andor SR-500i Raman spectrometer using a 532 nm laser source. The specific surface areas of the nanocomposites were obtained using the N_2 physisorption apparatus (JW-BK122W). The atomic content ratio of Co and S in the cobalt sulfide was determined by inductively coupled plasma mass spectrometry (ICP-MS, Agilent 7800, USA).

2.3 Electrochemical measurement

Cyclic voltammetry (CV), galvanostatic charge/discharge (GCD) and electrochemical impedance spectroscopy (EIS) of $CoS_{1.29}$@CNTs and $CoS_{1.29}$ electrodes were measured using CHI 660E workstation (Shanghai Chenhua, China). For three electrodes system test, the electrolyte was 2 M KOH aqueous solution. Reference electrode and counter electrode were Hg/HgO and Pt foil, respectively. The working electrode was prepared by coating electrode slurry in ethanol (80 wt% active material, 10 wt% carbon black and 10 wt% polytetrafluoroethylene) on Ni foam, and

dried at 60℃ in a vacuum oven for 12 h. Then the working electrode was obtained by pressed at 10 MPa for 1 min. A typical mass loading of the working electrodes was about 2.0 mg cm^{-2} and each electrode has an area of 1.0 ×1.0 cm^{-2}. The CV was recorded with the potential scan rates ranging from 5~50 mV s^{-1}. The EIS was conducted at open circuit voltage with an amplitude of 5 mV over the frequency range of 0.01~10^5 Hz. The specific capacitance of electrodes can be calculated according to the GCD curves based on the following equation [28]:

$$Q = \frac{I \times t}{m \times 3.6} \quad (1)$$

where Q is the specific capacitance (mAh g^{-1}), I is the discharge current (mA), t is the discharge time (s) and m is the mass of the electrode materials (mg).

In addition, an asymmetric supercapacitor (ASC) device was assembled to further study the electrochemical capacitive performance of the cobalt sulfide and carbon nanotubes. $CoS_{1.29}$@CNTs-6.1% on Ni foam (1×1 cm^{-2}) was used as the positive electrode and activated carbon (AC) on Ni foam was used as the negative electrode. The electrolyte was 2M KOH. The weight ratio of the active materials for the negative electrode and positive electrode was calculated on the charge balance theory, according to the following equation [29]:

$$\frac{m_+}{m_-} = \frac{Q_-}{Q_+} \quad (2)$$

where m is the mass, Q is the specific capacitance for positive and negative electrodes.

The specific capacitance (Q_d, mAh g^{-1}), energy density (E, Wh kg^{-1}) and power density (P, W kg^{-1}) of the ASC device were calculated based on the total mass of the electrode materials according the following equations [30, 31].

$$Q_d = \frac{I \times t}{M \times 3.6} \quad (3)$$

$$E = \frac{Q_d \times \Delta V}{2} \quad (4)$$

$$P = \frac{E \times 3600}{t} \quad (5)$$

where M is the total mass of the positive and negative electrodes (mg) and ΔV is the potential window (V). All the electrochemical tests of ASC device were performed in a two-electrode configuration at room temperature.

3. Results and discussion

3.1 Materials characterization

A typical synthesis process of cobalt sulfide@CNTs composites is shown in Fig. 1. After hydrothermal reaction process, the carbon nanotubes were directly combined with the Co-precursor. Then, the cobalt sulfide@CNTs composites were obtained using the ion-exchange process in Na_2S (as the sulfur source) solution at 80 ^oC for 24 hrs. The XRD spectra of Co-precursor and cobalt sulfide are displayed in Fig. 2. In the XRD spectrum of Co-precursor, all peaks are indexed to $Co_2(CO_3)(OH)_2$ (JCPDS card No. 29-1416), indicating the Co-precursor is $Co_2(CO_3)(OH)_2$ [32]. However, not any diffraction peak appears in the XRD spectrum of cobalt sulfide, meaning that the cobalt sulfide is amorphous.

Figs. 3a and 3b present the SEM images of pure cobalt sulfide and cobalt sulfide@CNTs-6.1%, respectively. The pure cobalt sulfide has an irregular blocky shape and many of small particles are existed on its surface. For the cobalt sulfide@CNTs-6.1% composite, the CNTs (marked with green color) were embedded inside the cobalt sulfide particles as shown in Fig. 3b. The CNTs in the cobalt sulfide

particles can provide many effective paths for electrolyte ions diffusion and charges transport [16]. Therefore, the cobalt sulfide@CNTs have improved ion diffusion and charge transport rates and thus enhanced the electrochemical performance. The CNTs combined with the cobalt sulfide particles were further characterized using TEM. As shown in Figs. 3c and 3d, the average diameter of the cobalt sulfide particles appears to be ~100 nm, and the CNTs are existed obviously in the cobalt sulfide particles. The corresponding SAED patterns shown in the inset of Fig. 3c has no ring patterns, confirming the amorphous characteristic of cobalt sulfide@CNTs-6.1%. In order to further reveal the morphological microstructures of the cobalt sulfide@CNTs-6.1% composite, the HRTEM image was measured and shown in Fig 3e. There are no regular lattice fringes can be found in the HRTEM image, which further proves that the cobalt sulfide is amorphous in the composite. Fig. 3f shows EDX mapping of the cobalt sulfide@CNTs-6.1% composite including three elements with carbon (O), sulfur (S) and cobalt (Co). It can be seen that the CNTs are embedded inside the cobalt sulfide particles and the elements of Co and S are uniformly distributed. Moreover, the atomic content ratio of Co and S can be obtained and it is 1:1.32. Furthermore, the accurate atomic content ratio of Co and S in cobalt sulfide was measured is 1:1.29 by the ICP-MS. Therefore, the molecular formula of cobalt sulfide is expressed as $CoS_{1.29}$.

The XPS spectra of $CoS_{1.29}$@CNTs-6.1% in Fig. 4 can be used to investigate the chemical composition and chemical states on the surface. The XPS survey spectrum of $CoS_{1.29}$@CNTs-6.1% is shown in Fig. 4a, and the peaks of Co, C, S and O can be obviously observed. The O element may come from the oxygen-containing functional

group on the material surface [3, 33]. The high-resolution spectrum of Co 2p in Fig. 4b can be deconvoluted into two satellite peaks and four spinorbit doublets, which indicate the characteristics of Co^{2+} and Co^{3+} in $CoS_{1.29}$ [34, 35]. The peaks at the binding energies of 794.4 and 779.3 eV are attributed to Co^{3+}, while the peaks at 798.0 and 782.1 eV can be assigned to Co^{2+} [36]. The peaks of 786.6 eV and 803.4 eV are the satellite peaks of Co^{2+} and Co^{3+}. For the spectrum of S 2p shown in Fig. 4c, the peaks at 162.7 and 164.6 eV belong to S $2p_{2/3}$ and S $2p_{1/2}$, respectively. Moreover, the peak at 169.4 eV is assigned to the shake-up satellite peak of S 2p. The XPS spectrum of C 1s in Fig. 4d can be deconvoluted into three peaks at 284.8, 285.8 and 287.2 eV. The peaks at 284.8 eV can be attributed to C=C in the CNTs, and the peaks at 285.8 and 287.2 eV are corresponding to C−O and C=O bonds on the surfaces of CNTs [37, 38].

Raman spectroscopy results of the $CoS_{1.29}$@CNTs-6.1% composite, CNTs and $CoS_{1.29}$ are shown in Fig. 5a. The four peaks at 476, 512, 604 and 672 cm^{-1} in the spectrums of $CoS_{1.29}$@CNTs-6.1% and $CoS_{1.29}$ are corresponding to the Raman characteristics of cobalt sulfide [39, 40]. In addition, three peaks are also clearly observed in the spectrum of $CoS_{1.29}$@CNTs-6.1% at 1347, 1578 and 2678 cm^{-1}, which are corresponding to the typical D, G and 2D bands of the carbon nanotubes. The D band with A_{1g} symmetry is attributed to the defects and sp^3 bonding, while the G band with E_{2g} symmetry belongs to in-plane bond-stretching motion of sp^2 C pairs [41]. The 2D band is originated from the momentum conservation process of the CNTs [42]. For comparison, the Raman spectrum of pure CNTs have also been tested. It can be seen that the I_D/I_G intensity ratio is increased from 0.46 in the pure CNTs to 0.63 in the $CoS_{1.29}$@CNTs-

6.1% composite. The higher I_D/I_G intensity ratio suggests the higher disorders and defects in carbon nanotubes, which is resulted from the combined with CNTs in the $CoS_{1.29}$ in the hydrothermal reaction process [40].

To further investigate the functional groups on the surface of $CoS_{1.29}$, CNTs and $CoS_{1.29}$@CNTs-6.1%, FT-IR spectrum has been obtained within the region from 400 to 4000 cm^{-1} and the result is shown in Fig. 5b. The vibration peak related to O−H bonding are observed in the spectrums of $CoS_{1.29}$, CNTs and $CoS_{1.29}$@CNTs-6.1% at 3437 and 1632 cm^{-1}, indicating that there are many hydroxyl groups on the surface of all samples [43, 44]. The peak at 2169 cm^{-1} is belonged to the carbon dioxide in the air. The peak at 1384 cm^{-1} in the spectra of $CoS_{1.29}$@CNTs-6.1% and pure CNTs are attributed to the stretching vibration C−OH modes from the CNTs [18, 45]. The Co=S stretching mode is observed at 1128 cm^{-1} in the spectra of $CoS_{1.29}$ and $CoS_{1.29}$@CNTs-6.1%, indicating the presence of cobalt sulfide in the as-prepared composites [4]. And the peak at 584 cm^{-1} is attributed to the lattice vibrations of Co=S [46].

3.2 Electrochemical performance

The CV, GCD and EIS of the electrode materials were tested in the three electrodes system with an electrolyte concentration of 2 M KOH. Fig. 6a shows the CV curves of the $CoS_{1.29}$, $CoS_{1.29}$@CNTs-2.5%, $CoS_{1.29}$@CNTs-6.1% and $CoS_{1.29}$@CNTs-9.5% at a scan rate of 10 mV s^{-1} in the potential window of 0~0.6 V. It can be clearly observed that there are a pair of distinct redox peaks in all the CV curves, indicating that the capacitance is mainly based on the reversible Faradaic redox mechanism as shown in the following redox reaction [47, 48]:

$$CoS_{1.29} + OH^- \leftrightarrow CoS_{1.29}OH + e^- \quad (6)$$

$$CoS_{1.29}OH + OH^- \leftrightarrow CoS_{1.29}O + H_2O + e^- \quad (7)$$

Moreover, the peak current and closed area of the $CoS_{1.29}$@CNTs-6.1% composite are larger than those of $CoS_{1.29}$, $CoS_{1.29}$@CNTs-2.5% and $CoS_{1.29}$@CNTs-9.5%, which suggest that the $CoS_{1.29}$@CNTs-6.1% electrode has the highest capacity among these four electrodes [49].

Fig. 6b displays the GCD curves of the above four electrodes tested at a current density of 1 A g^{-1}. It can be seen that the $CoS_{1.29}$@CNTs-6.1% electrode exhibits the longest discharge time. This result further confirms that the $CoS_{1.29}$@CNTs-6.1% electrode has a higher capacity than those of the $CoS_{1.29}$, $CoS_{1.29}$@CNTs-2.5% and $CoS_{1.29}$@CNTs-9.5%. Therefore, the addition of 6.1 wt% CNTs in the $CoS_{1.29}$ can significantly enhance the capacitance of supercapacitor electrode.

Fig. 6c shows the CV curves of $CoS_{1.29}$@CNTs-6.1% at different scan rates. As the scan rate is increased from 5 to 50 mV s^{-1}, the peaks currents are gradually increased, and the oxidation and reduction peak positions are slightly moved to positive and negative potentials, respectively. This is mainly corresponding to the polarization effect of the electrode [50]. In addition, the redox peak can be observed at a much higher scan rate of 50 mV s^{-1}, suggesting the good capacitive behavior of $CoS_{1.29}$@CNTs-6.1%.

To further investigate the electrochemical performance of $CoS_{1.29}$@CNTs-6.1%, the GCD studies were performed at different current densities from 1 to 8 A g^{-1} within in a fixed potential window of 0~0.5 V and the results are shown in Fig. 6d. Because of the Faradaic redox of pseudocapacitor, obvious voltage platforms are formed in all GCD

curves which agrees well with the results from the CV analysis. Therefore, all the above results indicate that the composite electrode of $CoS_{1.29}$@CNTs-6.1% has an excellent reversible redox property and a good electrochemical capacitive characteristic [51]. Based on the discharging times at various current densities, the specific capacitances of electrodes have been calculated according to Eq. (1). Fig. 6e shows the specific capacities of the $CoS_{1.29}$, $CoS_{1.29}$@CNTs-2.5%, $CoS_{1.29}$@CNTs-6.1% and $CoS_{1.29}$@CNTs-9.5% composites at various current densities. It can be found that the specific capacitance of $CoS_{1.29}$@CNTs-6.1% electrode is much higher than those of the other three electrodes. For example, at the current density of 1 A g^{-1}, the specific capacitance of the $CoS_{1.29}$@CNTs-6.1% electrode is 99.7 mAh g^{-1}, but they are only 84.1, 74.1 and 70.5 mAh g^{-1} for $CoS_{1.29}$, $CoS_{1.29}$@CNTs-2.5% and $CoS_{1.29}$@CNTs-9.5% composites, respectively.

Compared with that of the $CoS_{1.29}$, the significantly increased specific capacitance of the $CoS_{1.29}$@CNTs-6.1% can be attributed to the optimum concentration of carbon nanotubes in the nanocomposites, which introduce more paths for ion and electron transports and are beneficial to the transfer of electrolyte ions and electrons during the energy storage process. Moreover, the addition of CNTs in the hydrothermal reaction process can result in the formation of smaller $CoS_{1.29}$ nanoparticles and significantly increase the large specific surface areas of the $CoS_{1.29}$@CNTs-6.1% composite (10.9 m^2 g^{-1}) compared with those of the pristine $CoS_{1.29}$ (1.7 m^2 g^{-1}). The larger specific surface area can provide more active sites for the Faradaic redox reaction process to obtain larger capacitances [52]. At different current densities of 1, 2, 4, 6 and 8 A g^{-1}, the

specific capacitances of the $CoS_{1.29}$@CNTs-6.1% electrode are 99.7, 95.2, 90.6, 87.3 and 84.7 mAh g^{-1}, respectively. The decrease of capacitances with the increase of current density can be attributed to the suppressed diffusion/transportation of electrolytic ions at a higher current density [53].

The EIS spectra of $CoS_{1.29}$, $CoS_{1.29}$@CNTs-2.5%, $CoS_{1.29}$@CNTs-6.1% and $CoS_{1.29}$@CNTs-9.5% electrodes in the frequency range between 100 kHz and 0.01 Hz are shown in Fig. 6f. These spectra are straight lines at a lower frequency region and then semicircles at a higher frequency region. The slope of the inclined line in the lower frequency region represents the Warburg impedance (W), which is attributed to the ion diffusion in the electrolyte to the electrode interface [54]. The intercept points to the axis of the semicircles in the higher frequency range represents series resistance (R_s), and the diameter of the semicircle is related to charge-transfer resistance (R_{ct}) [55].

It found that the R_{ct} value of the $CoS_{1.29}$@CNTs-6.1% is 0.31 Ω, which are lower than that of $CoS_{1.29}$@CNTs-2.5% (0.37 Ω), $CoS_{1.29}$@CNTs-9.5% (0.46 Ω) and $CoS_{1.29}$ (0.78 Ω). The lowest charge-transfer resistance indicates that the $CoS_{1.29}$@CNTs-6.1% electrode has an outstanding charge-transfer kinetics. Moreover, the inclined line of the $CoS_{1.29}$@CNTs-6.1% electrode is much steeper in the lower frequency region than that of other electrodes, which proves that the $CoS_{1.29}$@CNTs-6.1% electrode has the shortest diffusion path length of the ions [56]. The reduced ion diffusion paths produced by carbon nanotubes effectively enhance the ion diffusion rates, which are beneficial to the increase of capacity. Therefore, due to the highest charge-transfer and ions diffusion rates, the $CoS_{1.29}$@CNTs-6.1% has the largest capacitance among these samples.

However, for the $CoS_{1.29}$@CNTs-2.5% and $CoS_{1.29}$@CNTs-9.5%, although the charge transfer and ion diffusion path length are lower than those of the pure $CoS_{1.29}$. But the series resistance of the $CoS_{1.29}$@CNTs-2.5% and $CoS_{1.29}$@CNTs-9.5% are 1.14 and 1.16 Ω respectively, which are larger than 1.01 of $CoS_{1.29}$. On the other hand, because the capacity of pure CNTs is much lower than that of cobalt sulfide [57], the presence of CNTs reduces the specific capacity of $CoS_{1.29}$@CNTs electrode materials. Especially, there are the large amount of CNTs in the $CoS_{1.29}$@CNTs-9.5% composite. Therefore, according to the above two reasons, the $CoS_{1.29}$@CNTs-2.5% and $CoS_{1.29}$@CNTs-9.5% show lower capacity than pure $CoS_{1.29}$.

3.3 Electrochemical properties of ASC device

An asymmetric supercapacitor (ASC) device was assembled to evaluate the electrochemical performance and demonstrate the practical application of the $CoS_{1.29}$@CNTs-6.1%. The $CoS_{1.29}$@CNTs-6.1% and active carbon (AC) were used as the positive and negative electrode materials, respectively, in an electrolyte of 2 M KOH aqueous solution. In order to achieve the charge balance of ASC device, the appropriate load ratio of the positive and negative electrodes was selected to be 1:2.27 based on the calculation using Eq. (2), which is 2.0 and 4.5 mg, respectively. Fig. 7a presents the CV curves of $CoS_{1.29}$@CNTs-6.1% and AC in different potential windows at a scan rate of 10 mV s^{-1}. It can be seen that the potential windows of $CoS_{1.29}$@CNTs-6.1% and AC are 0~0.6 V and -1~0 V, respectively, indicating that the ASC devices assembled by $CoS_{1.29}$@CNTs-6.1% composite and AC can be operated at a potential window of 0~1.6 V. Fig. 7b shows the CV curves of the $CoS_{1.29}$@CNTs-6.1%//AC asymmetric device in

different voltage ranges from 0.6 to 1.6 V at 50 mV s^{-1}. These CV curves have obvious redox peaks and no polarization occurs within 1.6 V. Thus, the potential window of 0~1.6 V is appropriate to investigate the electrochemical performance of the ASC device.

The GCD curves of $CoS_{1.29}$@CNTs-6.1%//AC device at a current density of 1 A g^{-1} and different potential windows are shown in Fig. 7c, which shows that the maximum voltage that the device can be charged is 1.6 V. The CV curves of the $CoS_{1.29}$@CNTs-6.1%//AC at different scan rates between 5~50 mV s^{-1} are illustrated in Fig. 7d. The CV loops of the $CoS_{1.29}$@CNTs-6.1%//AC exhibit irregular shapes, indicating that the devices have a pseudocapacitive feature. Fig. 7e shows the GCD results of the $CoS_{1.29}$@CNTs-6.1%//AC device at different current densities in a voltage range of 0~1.6 V. The quasi-triangular shape at all the curves indicates a good coulombic efficiency with good capacitive behavior and reversibility [58]. Moreover, the ASC device has a maximum specific capacitance of 48.9 mAh g^{-1} at 0.5 A g^{-1} and it still remains a value of 32.1 mAh g^{-1} as the current density is increases to 5 A g^{-1}. The energy density and power density of the $CoS_{1.29}$@CNTs-6.1%//AC device are shown in Fig. 7f. The maximum energy density is 39.1 Wh kg^{-1} at a power density of 399.9 W kg^{-1}. Even at a high power density of 4000.7 W kg^{-1}, the ASC device still retains an energy density of 25.7 Wh kg^{-1}. Which is superior to that of many reported ASC devices, such as $CoS_{1.097}$//AC (33.4 Wh kg^{-1} at 750.0 W kg^{-1}) [59], Co_9S_8//AC (20.0 Wh kg^{-1}at 828.5 W kg^{-1}) [1], CoS//AC (37.0 Wh kg^{-1}at 240.0 W kg^{-1}) [60] and CoS_2/rGO//AC (13.8 Wh kg^{-1}at 824.6 W kg^{-1}) [20].

To investigate the stability of the device, the cycle performances of the $CoS_{1.29}$@CNTs-6.1%//AC and $CoS_{1.29}$//AC ASC devices was continuously tested at a current density of 3 A g^{-1} for 2000 cycles of GCD, and the obtained results are shown in Fig. 8a. After 2000 cycles, the residual specific capacitance of the $CoS_{1.29}$@CNTs-6.1%//AC device is about 91.3 % of the initial value. which is higher than the $CoS_{1.29}$//AC device (82.7%), indicating the excellent cycle stability of the $CoS_{1.29}$@CNTs-6.1%//AC ASC device, and the improves the stability of electrode material due to the presence of CNTs. Fig. 8b shows the Nyquist plot of the $CoS_{1.29}$@CNTs-6.1%//AC device before and after 2000 cycles. The values of R_s and R_{ct} before cycles are 2.30 Ω and 0.93 Ω, and these values after 2000 cycles are changed to 2.35 Ω and 2.13 Ω, respectively. It can be found that the R_s values of the device have not shown significant changes, although the R_{ct} values are only increased slightly, which indicates that the activity of the $CoS_{1.29}$@CNTs-6.1% composite does not show any significant changes during the cycles.

4. Conclusion

In summary, the $CoS_{1.29}$@CNTs-6.1% composites were successfully synthesized via a facile hydrothermal and ion-exchange process. They showed good electrochemical performance to be used as positive electrode for supercapacitor. The addition of carbon nanotubes is an effective method to improve the electrochemical performance of cobalt sulfide. When the contents of CNTs was increased to 6.1%, the specific capacitance of $CoS_{1.29}$@CNTs composite was enhanced to 99.7 mAh g^{-1} from 84.1 mAh g^{-1} of the pristine $CoS_{1.29}$ at 1 A g^{-1}. Furthermore, the assembled asymmetric supercapacitor

showed an good cycling performance (91.3 % capacitance retention after 2000 cycles) and excellent energy and power density (39.1 Wh kg^{-1} at 399.9 W kg^{-1}). Thus, the as-prepared $CoS_{1.29}$@CNTs-6.1% composite is a promising cathode material for application in asymmetric supercapacitor.

Acknowledgements

Funding supports from UK Engineering Physics and Science Research Council (EPSRC EP/P018998/1), Newton Mobility Grant (IE161019) through Royal Society and NFSC, and Royal academy of Engineering UK-Research Exchange with China and India are acknowledged.

References

1. X. Han, K. Tao, D. Wang and L. Han, *Nanoscale*, 2018, **10**, 2735-2741.
2. G. Liu, B. Wang, T. Liu, L. Wang, H. Luo, T. Gao, F. Wang, A. Liu and D. Wang, *J. Mater. Chem. A*, 2018, **6**, 1822-1831.
3. Y. Zhu, H. Chen, S. Chen, C. Li, M. Fan and K. Shu, *J. Mater. Sci.*, 2018, **53**, 6157-6169.
4. M. Jin, S.-Y. Lu, L. Ma, M.-Y. Gan, Y. Lei, X.-L. Zhang, G. Fu, P.-S. Yang and M.-F. Yan, *J. Power Sources*, 2017, **341**, 294-301.
5. J. Zhu, L. Xiang, D. Xi, Y. Zhou and J. Yang, *Bull. Mater. Sci.*, 2018, **41**, 54.
6. S. Hussain, E. Kovacevic, R. Amade, J. Berndt, C. Pattyn, A. Dias, C. Boulmer-Leborgne, M.-R. Ammar and E. Bertran-Serra, *Electrochim. Acta*, 2018, **268**, 218-225.
7. L.-l. Liu, K. P. Annamalai and Y.-s. Tao, *New Carbon Mater.*, 2016, **31**, 336-342.
8. S.-Y. Zhai, L.-L. Li and M.-G. Wang, *Ionics*, 2017, **23**, 1819-1830.

9. H. Wang, M. Liang, D. Duan, W. Shi, Y. Song and Z. Sun, *Chem. Eng. J.*, 2018, **350**, 523-533.

10. L. Wang, J. Liu, L. L. Zhang, B. Dai, M. Xu, M. Ji, X. S. Zhao, C. Cao, J. Zhang and H. Zhu, *RSC Adv.*, 2015, **5**, 8422-8426.

11. Y. Sui, H. Hu, J. Qi, Y. Zhou, F. Wei, Y. He, Q. Meng, Y. Ren and Z. Sun, *J. Mater. Sci-Mater. El*, 2018, **29**, 11187-11198.

12. Y.-P. Gao, K.-J. Huang, X. Wu, Z.-Q. Hou and Y.-Y. Liu, *J. Alloy. Compd.*, 2018, **741**, 174-181.

13. X. Li, J. Sun, L. Feng, L. Zhao, L. Ye, W. Zhang and L. Duan, *J. Alloy. Compd.*, 2018, **753**, 508-516.

14. X. Hou, T. Peng, J. Cheng, Q. Yu, R. Luo, Y. Lu, X. Liu, J.-K. Kim, J. He and Y. Luo, *Nano Res.*, 2017, **10**, 2570-2583.

15. A. G. Tabrizi, N. Arsalani, Z. Naghshbandi, L. S. Ghadimi and A. Mohammadi, *Int. J. Hydrogen Energ.*, 2018, **43**, 12200-12210.

16. J.-h. Liu, X.-y. Xu, W. Lu, X. Xiong, X. Ouyang, C. Zhao, F. Wang, S.-y. Qin, J.-l. Hong, J.-n. Tang and D.-Z. Chen, *Electrochim. Acta*, 2018, **283**, 366-373.

17. W. Xu, J. Lu, W. Huo, J. Li, X. Wang, C. Zhang, X. Gu and C. Hu, *Nanoscale*, 2018, **10**, 14304-14313.

18. R. Hu, J. Zhao, G. Zhu and J. Zheng, *Electrochim. Acta*, 2018, **261**, 151-159.

19. S. Liu, Y. Zhao, B. Zhang, H. Xia, J. Zhou, W. Xie and H. Li, *J. Power Sources*, 2018, **381**, 116-126.

20. Q. Chen, D. Cai and H. Zhan, *J. Alloy. Compd.*, 2017, **706**, 126-132.

21. F. Cao, M. Zhao, Y. Yu, B. Chen, Y. Huang, J. Yang, X. Cao, Q. Lu, X. Zhang, Z. Zhang, C. Tan and H. Zhang, *J Am Chem Soc*, 2016, **138**, 6924-6927.

22. D. Jiang, Q. Xu, S. Meng, C. Xia and M. Chen, *J. Alloy. Compd.*, 2017, **706**, 41-47.

23. F. Ochai-Ejeh, M. J. Madito, K. Makgopa, M. N. Rantho, O. Olaniyan and N. Manyala, *Electrochim. Acta*, 2018, **289**, 363-375.

24. A. Mohammadi, N. Arsalani, A. G. Tabrizi, S. E. Moosavifard, Z. Naqshbandi and L. S. Ghadimi, *Chem. Eng. J.*, 2018, **334**, 66-80.

25. M. Mao, L. Mei, L. Wu, Q. Li and M. Zhang, *RSC Adv.*, 2014, **4**, 12050.

26. C.-Y. Chen, Z.-Y. Shih, Z. Yang and H.-T. Chang, *J. Power Sources*, 2012, **215**, 43-47.

27. R. Bhatia and V. Prasad, *Solid State Commun.*, 2010, **150**, 311-315.

28. S. K. Shinde, M. B. Jalak, S. Y. Kim, H. M. Yadav, G. S. Ghodake, A. A. Kadam and D. Y. Kim, *Ceram. Int.*, 2018, **44**, 23102-23108.

29. M. Guo, J. Balamurugan, T. D. Thanh, N. H. Kim and J. H. Lee, *J. Mater. Chem. A*, 2016, **4**, 17560-17571.

30. Y. Liu, G. Jiang, S. Sun, B. Xu, J. Zhou, Y. Zhang and J. Yao, *J. Alloy. Compd.*, 2018, **731**, 560-568.

31. C. R. Rawool, S. P. Karna and A. K. Srivastava, *Electrochim. Acta*, 2019, **294**, 345-356.

32. M. Roy, S. Ghosh and M. K. Naskar, *Dalton T.*, 2014, **43**, 10248-10257.

33. K. Krishnamoorthy, G. K. Veerasubramani and S. J. Kim, *Mat. Sci. Semicon. Proc.*, 2015, **40**, 781-786.

34. X. Wu, L. Jiang, C. Long, T. Wei and Z. Fan, *Adv. Funct. Mater.*, 2015, **25**, 1648-1655.

35. Y. Lu, L. Li, D. Chen and G. Shen, *J. Mater. Chem. A*, 2017, **5**, 24981-24988.

36. Y. Liu, G. Jiang, S. Sun, B. Xu, J. Zhou, Y. Zhang and J. Yao, *J. Electroanal. Chem.*, 2017, **804**, 212-219.

37. Y. Zou, C. Cai, C. Xiang, P. Huang, H. Chu, Z. She, F. Xu, L. Sun and H.-B. Kraatz, *Electrochim. Acta*, 2018, **261**, 537-547.

38. D. H. Suh, S. K. Park, P. Nakhanivej, Y. Kim, S. M. Hwang and H. S. Park, *J. Power Sources*, 2017, **372**, 31-37.

39. E. Aslan, I. Akin and I. H. Patir, *Chem. Eur. J.*, 2016, **22**, 5342-5349.

40. J. Huo, J. Wu, M. Zheng, Y. Tu and Z. Lan, *Electrochim. Acta*, 2016, **187**, 210-217.

41. A. Pendashteh, E. Senokos, J. Palma, M. Anderson, J. J. Vilatela and R. Marcilla, *J. Power Sources*, 2017, **372**, 64-73.

42. A. C. Ferrari and D. M. Basko, *Nat Nanotechnol*, 2013, **8**, 235-246.

43. R. Yuksel, N. Uysal, A. Aydinli and H. E. Unalan, *J. Electrochem. Soc.*, 2018, **165**, A283-A290.

44. S. M. Pourmortazavi, M. Rahimi-Nasrabadi, B. Larijani, M. S. Karimi and S. Mirsadeghi, *J. Mater. Sci-Mater. El*, 2018, **29**, 13833-13841.

45. B. S. Singu and K. R. Yoon, *Electrochim. Acta*, 2018, **268**, 304-315.

46. P. Liu, X. Chang, J. Lin, S. Yan, L. Yao, J. Lian, H. Lin and S. Han, *J. Mater. Sci.*, 2017, **53**, 759-773.

47. Y. Zhao, X. He, R. Chen, Q. Liu, J. Liu, J. Yu, J. Li, H. Zhang, H. Dong, M. Zhang and J. Wang, *Chem. Eng. J.*, 2018, **352**, 29-38.

48. S. Sahoo and C. S. Rout, *Electrochim. Acta*, 2016, **220**, 57-66.

49. S. Chen, H. Chen, C. Li, M. Fan, C. Lv, G. Tian and K. Shu, *J. Mater. Sci.*, 2017, **52**,

6687-6696.

50. L. Li, X. Liu, C. Liu, H. Wan, J. Zhang, P. Liang, H. Wang and H. Wang, *Electrochim. Acta*, 2018, **259**, 303-312.

51. Z. Yu, Z. Cheng, G. Tsekouras, X. Wang, X. Kong, M. Osada and S. X. Dou, *Electrochim. Acta*, 2018, **281**, 761-768.

52. Y. Zhu, X. Chen, W. Zhou, K. Xiang, W. Hu and H. Chen, *Electrochim. Acta*, 2017, **249**, 64-71.

53. A. Bera, A. Kumar Das, A. Maitra, R. Bera, S. Kumar Karan, S. Paria, L. Halder, S. Kumar Si and B. Bhusan Khatua, *Chem. Eng. J.*, 2018, **343**, 44-53.

54. G. A. M. Ali, M. M. Yusoff, H. Algarni and K. F. Chong, *Ceram. Int.*, 2018, **44**, 7799-7807.

55. S. Ramesh, D. Vikraman, H.-S. Kim, H. S. Kim and J.-H. Kim, *J. Alloy. Compd.*, 2018, **765**, 369-379.

56. X. Song, L. Tan, X. Wang, L. Zhu, X. Yi and Q. Dong, *J. Electroanal. Chem.*, 2017, **794**, 132-138.

57. G. Saeed, S. Kumar, N. H. Kim and J. H. Lee, *Chem. Eng. J.*, 2018, **352**, 268-276.

58. W. Xu, J. Wan, W. Huo, Q. Yang, Y. Li, C. Zhang, X. Gu and C. Hu, *Chem. Eng. J.*, 2018, **354**, 1050-1057.

59. S. Liu, C. Mao, Y. Niu, F. Yi, J. Hou, S. Lu, J. Jiang, M. Xu and C. Li, *ACS Appl. Mater. Inter.*, 2015, **7**, 25568-25573.

60. S. Zhang, C. Li, H. Xiao, G. Wei, Y. Zhou, Z. Wang, J. Zhang and C. An, *J. Nanopart. Res.*, 2017, **19**, 202.

Figure Captions

Figure 1. Schematic illustration of the fabrication process of cobalt sulfide@CNTs.

Figure 2. XRD spectra of (a) Co-precursor and (b) cobalt sulfide.

Figure 3. SEM images of (a) cobalt sulfide and (b) cobalt sulfide@CNTs-6.1%; (c, d) TEM image of cobalt sulfide@CNTs-6.1% (inset represent the corresponding SAED pattern); (e) HRTEM image of cobalt sulfide@CNTs-6.1%; (f) EDX mapping of cobalt sulfide@CNTs-6.1%.

Figure 4. (a) Full XPS spectrum of $CoS_{1.29}$@CNTs-6.1%; high-resolution XPS spectra of (b) Co 2p, (c) S 2p and (d) C 1s.

Figure 5. (a) Raman spectra of $CoS_{1.29}$@CNTs-6.1%, CNTs and $CoS_{1.29}$; (b) FT-IR spectra of $CoS_{1.29}$@CNTs-6.1%, $CoS_{1.29}$ and CNTs.

Figure 6. Electrochemical performances of $CoS_{1.29}$, $CoS_{1.29}$@CNTs-2.5%, $CoS_{1.29}$@CNTs-6.1% and $CoS_{1.29}$@CNTs-9.5% composites in three electrodes system. (a) CV curves at 10 mV s^{-1} and (b) GCD curves at 1 A g^{-1}; (c) CV curves and (d) GCD curves of the $CoS_{1.29}$@CNTs-6.1% electrode; (e) Relationship between specific capacity and current density; (f) Nyquist plots comparison between $CoS_{1.29}$, $CoS_{1.29}$@CNTs-2.5%, $CoS_{1.29}$@CNTs-6.1% and $CoS_{1.29}$@CNTs-9.5% electrodes.

Figure 7. (a) CV curves of $CoS_{1.29}$@CNTs-6.1% and AC electrodes at a scan rate of 10

mV s^{-1} in a three electrodes system; (b) CV curves of the device at a scan rate of 50 mV s^{-1} in different potential windows; (c) GCD curves of the device at a current density of 1 A g^{-1} in different potential windows; (d) CV curves of the device at a scan rate of 5~50 mV s^{-1}; (e) GCD curves of the device at a current density of 0.5~5 A g^{-1}; (f) Ragone plot of the ASC device.

Figure 8. (a) Cycling stabilities of the $CoS_{1.29}$@CNTs-6.1%//AC and $CoS_{1.29}$//AC devices (insert photograph of lighting LED bulb); (b) Nyquist plot of the $CoS_{1.29}$@CNTs-6.1%//AC device before and after 2000 cycles.

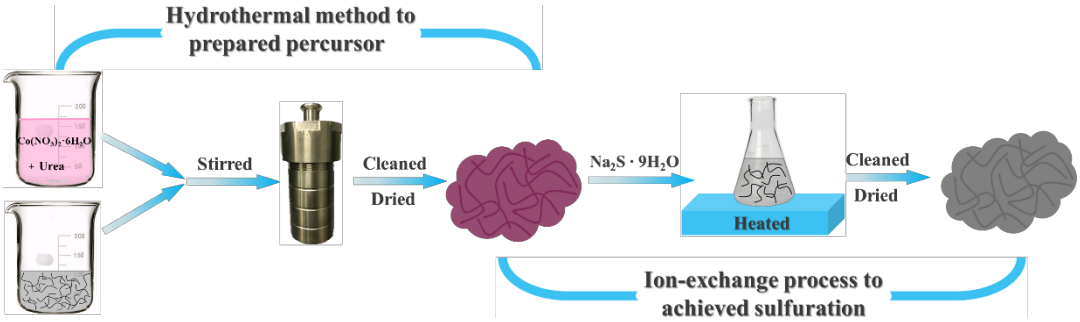
Hydrothermal method to
prepared percursor
$Co(NO_3)_2 \cdot 6H_2O$
+ Urea
Stirred
Cleaned
Dried
$Na_2S \cdot 9H_2O$
Heated
Cleaned
Dried
Ion-exchange process to
achieved sulfuration

Figure 1

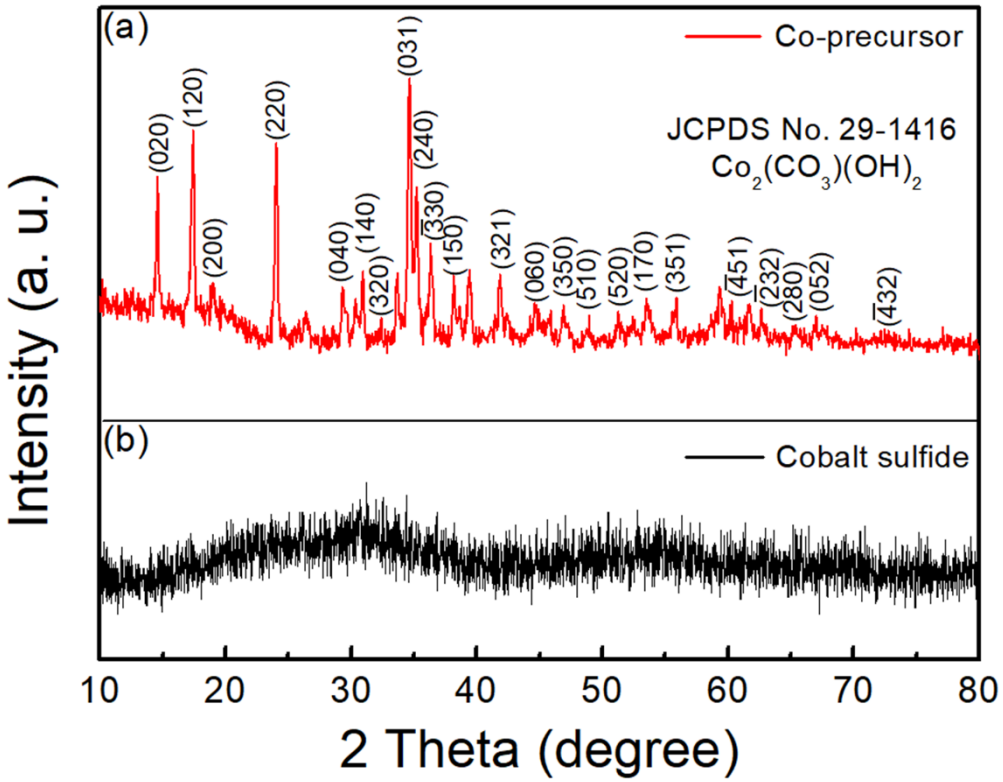
(a)
Co-precursor
JCPDS No. 29-1416
Co2(CO3)(OH)2
(020)
(120)
(200)
(220)
(040)
(140)
(320)
(031)
(240)
(330)
(150)
(321)
(060)
(350)
(510)
(520)
(170)
(351)
(451)
(232)
(280)
(052)
(432)
(b)
Cobalt sulfide
Intensity (a. u.)
10
20
30
40
50
60
70
80
2 Theta (degree)

Figure 2

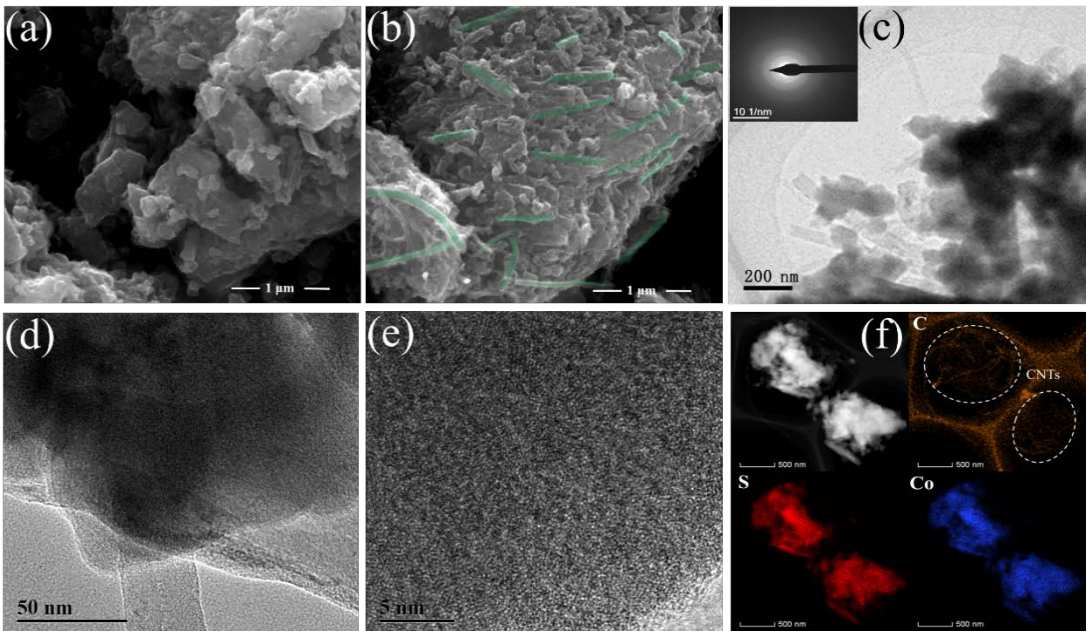
(a)
1 μm
(b)
1 μm
(c)
10 1/nm
200 nm
(d)
50 nm
(e)
5 nm
(f)
C
CNTs
500 nm
S
Co
500 nm
500 nm

Figure 3

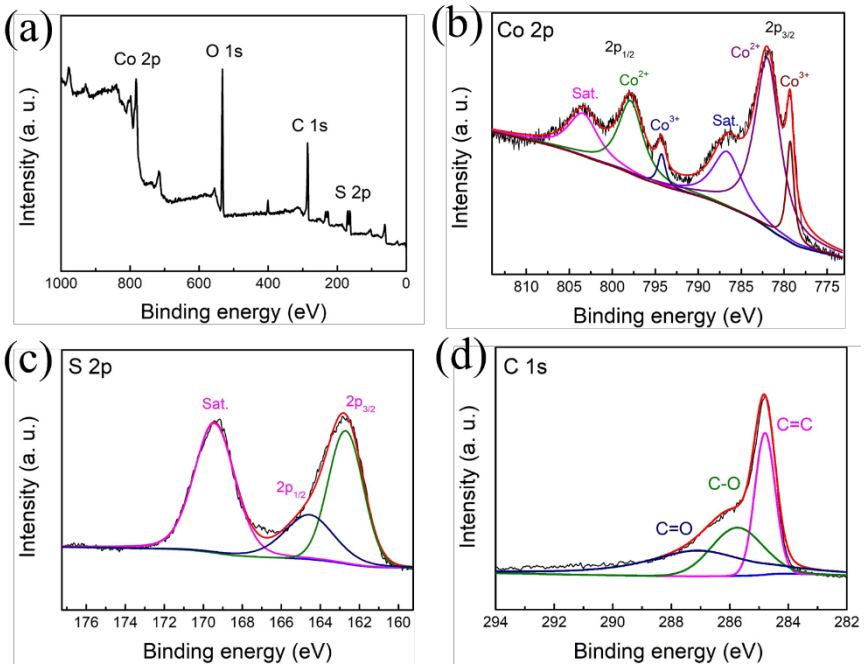
(a)
Co 2p
O 1s
C 1s
S 2p
Intensity (a. u.)
1000 800 600 400 200 0
Binding energy (eV)
(b)
Co 2p
2p1/2
2p3/2
Co2+
Co3+
Sat.
Sat.
Co2+
Co3+
Intensity (a. u.)
810 805 800 795 790 785 780 775
Binding energy (eV)
(c)
S 2p
Sat.
2p3/2
2p1/2
Intensity (a. u.)
176 174 172 170 168 166 164 162 160
Binding energy (eV)
(d)
C 1s
C=C
C-O
C=O
Intensity (a. u.)
294 292 290 288 286 284 282
Binding energy (eV)

Figure 4

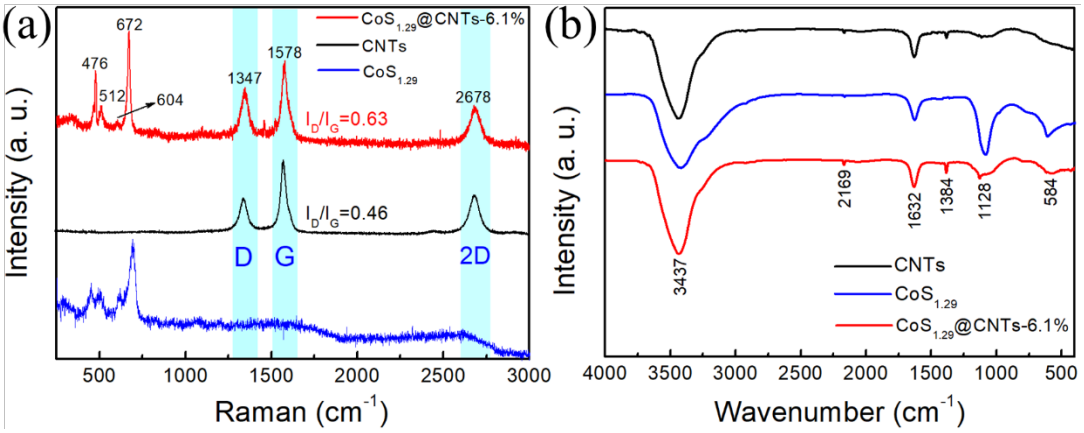
(a)
672
476
512
604
1347
1578
2678
CoS1.29@CNTs-6.1%
CNTs
CoS1.29
ID/IG=0.63
ID/IG=0.46
D
G
2D
Intensity (a. u.)
500
1000
1500
2000
2500
3000
Raman (cm-1)
(b)
3437
2169
1632
1384
1128
584
CNTs
CoS1.29
CoS1.29@CNTs-6.1%
Intensity (a. u.)
4000
3500
3000
2500
2000
1500
1000
500
Wavenumber (cm-1)

Figure 5

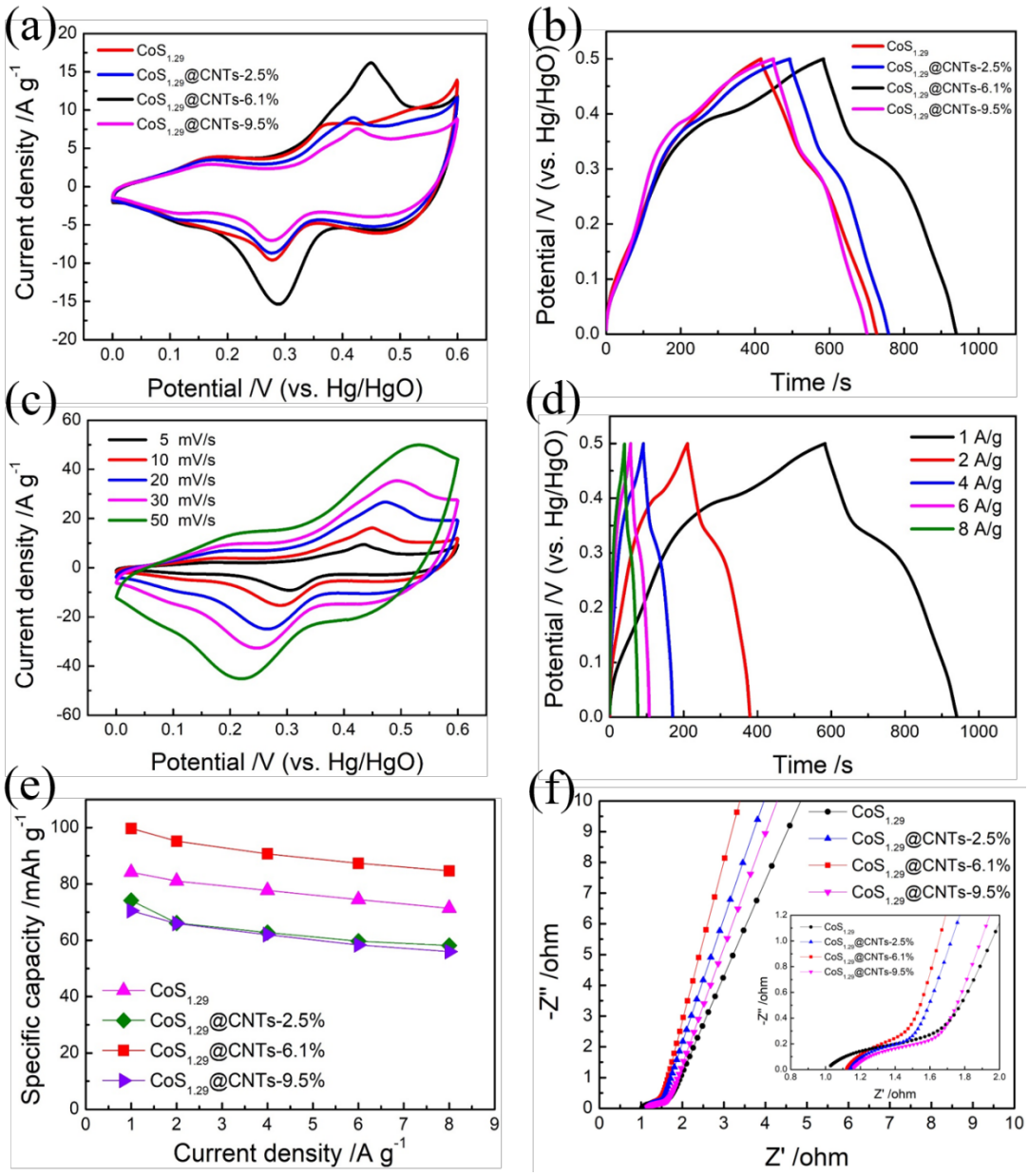
(a)
Current density /A g-1
Potential /V (vs. Hg/HgO)
CoS1.29
CoS1.29@CNTs-2.5%
CoS1.29@CNTs-6.1%
CoS1.29@CNTs-9.5%
(b)
Potential /V (vs. Hg/HgO)
Time /s
(c)
Current density /A g-1
Potential /V (vs. Hg/HgO)
5 mV/s
10 mV/s
20 mV/s
30 mV/s
50 mV/s
(d)
Potential /V (vs. Hg/HgO)
Time /s
1 A/g
2 A/g
4 A/g
6 A/g
8 A/g
(e)
Specific capacity /mAh g-1
Current density /A g-1
(f)
-Z'' /ohm
Z' /ohm

Figure 6

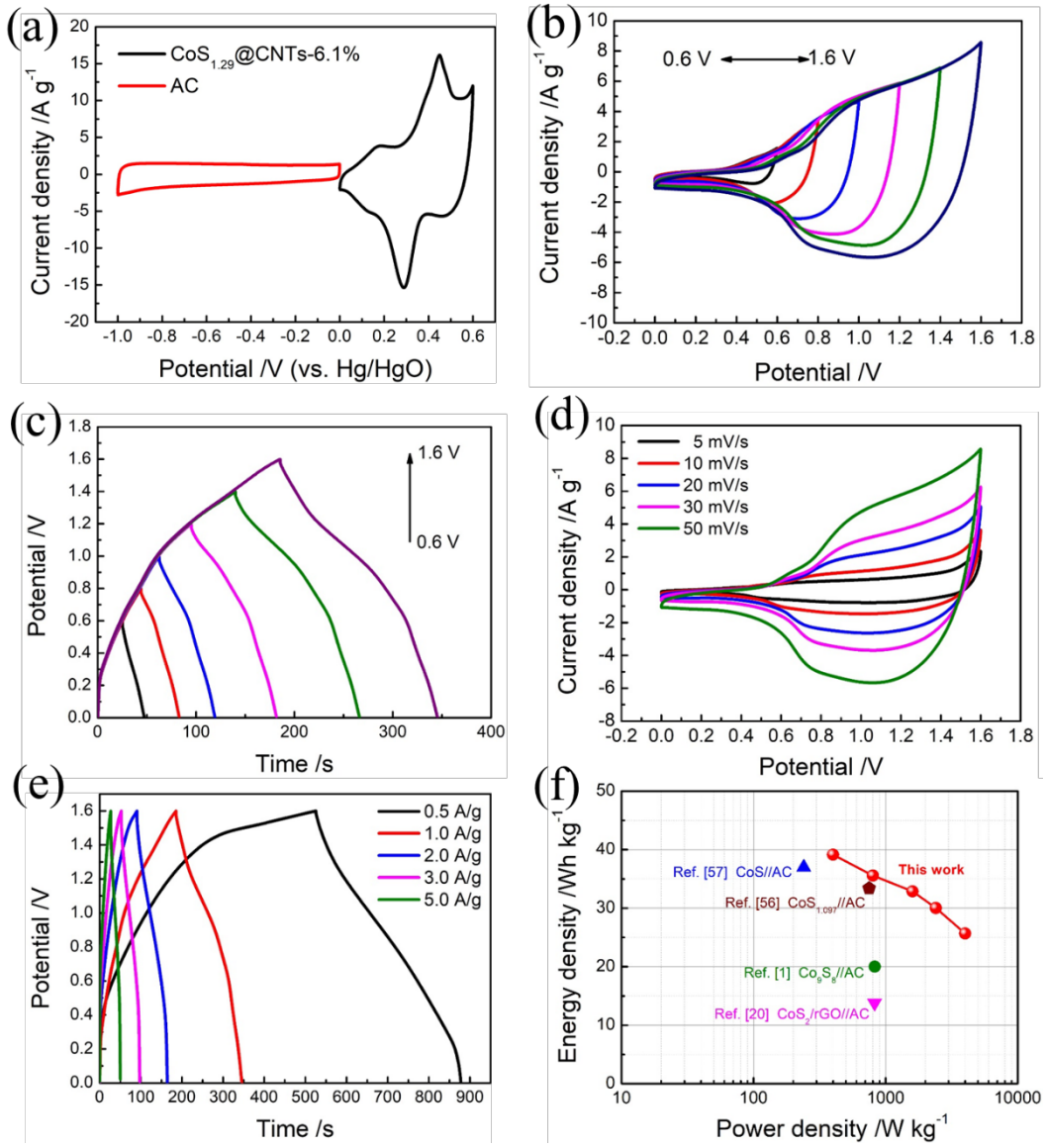
(a)
CoS1.29@CNTs-6.1%
AC
Current density /A g-1
Potential /V (vs. Hg/HgO)
(b)
0.6 V
1.6 V
Current density /A g-1
Potential /V
(c)
1.6 V
0.6 V
Potential /V
Time /s
(d)
5 mV/s
10 mV/s
20 mV/s
30 mV/s
50 mV/s
Current density /A g-1
Potential /V
(e)
0.5 A/g
1.0 A/g
2.0 A/g
3.0 A/g
5.0 A/g
Potential /V
Time /s
(f)
Ref. [57] CoS//AC
This work
Ref. [56] CoS1.097//AC
Ref. [1] Co9S8//AC
Ref. [20] CoS2/rGO//AC
Energy density /Wh kg-1
Power density /W kg-1

Figure 7

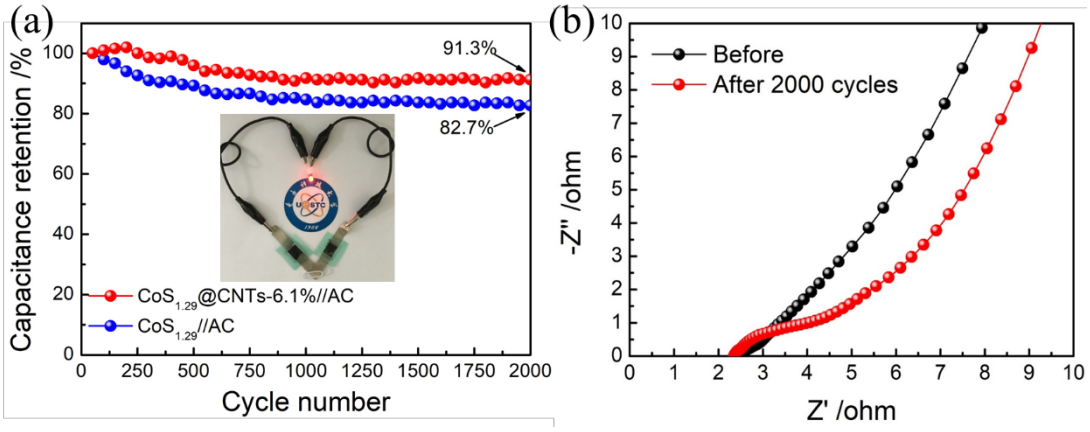
(a)
Capacitance retention /%
Cycle number
91.3%
82.7%
CoS1.29@CNTs-6.1%//AC
CoS1.29//AC
(b)
-Z'' /ohm
Z' /ohm
Before
After 2000 cycles

Figure 8